

Lawrence Berkeley National Laboratory

LBL Publications

Title

Resolution of Virtual Depth Sectioning from Four-Dimensional Scanning Transmission Electron Microscopy

Permalink

<https://escholarship.org/uc/item/0v9041pk>

Journal

Microscopy and Microanalysis, 29(4)

ISSN

1431-9276

Authors

Terzoudis-Lumsden, EWC

Petersen, TC

Brown, HG

et al.

Publication Date

2023-07-25

DOI

10.1093/micmic/ozad068

Copyright Information

This work is made available under the terms of a Creative Commons Attribution License, available at <https://creativecommons.org/licenses/by/4.0/>

Peer reviewed

Resolution of Virtual Depth Sectioning from Four-Dimensional Scanning Transmission Electron Microscopy

E W C Terzoudis-Lumsden, T C Petersen, H G Brown, P M Pelz, C Ophus, S D Findlay



Resolution of Virtual Depth Sectioning from Four-Dimensional Scanning Transmission Electron Microscopy

E.W.C. Terzoudis-Lumsden¹, T.C. Petersen^{1,2}, H.G. Brown³ , P.M. Pelz⁴, C. Ophus⁵, and S.D. Findlay^{1,*} 

¹School of Physics and Astronomy, Monash University, Melbourne, VIC 3800, Australia

²Monash Centre for Electron Microscopy, Monash University, Melbourne, VIC 3800, Australia

³Ian Holmes Imaging Center, Bio21 Molecular Science and Biotechnology Institute, University of Melbourne, Melbourne, VIC 3052, Australia

⁴Institute of Micro- and Nanostructure Research and Center for Nanoanalysis and Electron Microscopy, Friedrich-Alexander Universität Erlangen-Nürnberg, Erlangen, Bavaria 91058, Germany

⁵National Center for Electron Microscopy, Molecular Foundry, Lawrence Berkeley National Laboratory, Berkeley, CA 94720, USA

*Corresponding author: S.D. Findlay, E-mail: scott.findlay@monash.edu

Abstract

One approach to three-dimensional structure determination using the wealth of scattering data in four-dimensional (4D) scanning transmission electron microscopy (STEM) is the parallax method proposed by Ophus et al. (2019). Advanced phase reconstruction methods enabled by 4D scanning transmission electron microscopy, *Microsc Microanal* **25**, 10–11), which determines the scattering matrix and uses it to synthesize a virtual depth-sectioning reconstruction of the sample structure. Drawing on an equivalence with a hypothetical confocal imaging mode, we derive contrast transfer and point spread functions for this parallax method applied to weakly scattering objects, showing them identical to earlier depth-sectioning STEM modes when only bright field signal is used, but that improved depth resolution is possible if dark field signal can be used. Through a simulation-based study of doped Si, we show that this depth resolution is preserved for thicker samples, explore the impact of shot noise on the parallax reconstructions, discuss challenges to making use of dark field signal, and identify cases where the interpretation of the parallax reconstruction breaks down.

Key words: depth sectioning, parallax, scattering matrix, 3D imaging, 4D-STEM

Introduction

When characterizing material structure at atomic resolution via scanning transmission electron microscopy (STEM), a variety of scattering signals can be used to image the sample. Fast-readout pixel detectors now enable routine spatial mapping of diffraction patterns at speeds sufficient to outrun imaging instabilities (Ophus, 2019; MacLaren et al., 2020), giving access to scattering information supplied by the momentum degrees of freedom which were traditionally integrated over. This imaging paradigm is commonly referred to as 4D-STEM.

Momentum-resolved data in 4D-STEM affords new opportunities for reconstructing the sample potential (Müller et al., 2014; Jiang et al., 2018; Wen et al., 2019; Bustillo et al., 2021) from scattering information encoded in the phase, or fast mapping of specimen symmetries encoded in the scanned diffraction correlations (Liu et al., 2013; Krajnak & Etheridge, 2020). Since we can only directly measure electron beam intensity, phase retrieval techniques are needed to solve the inverse problem. Phase object methods where the electron scattering is assumed confined to a single plane include differential phase contrast (DPC) (Dekkers & De Lang, 1974; Müller et al., 2014; Lazić et al., 2016; Yücelen et al., 2018), ptychography (Yang et al., 2017; Rodenburg & Maiden, 2019), and holography (Gabor, 1948; Cowley, 1992; Lichte & Lehmann, 2007). Because the thickness range over which

the phase object approximation holds at atomic resolution is limited (Close et al., 2015; Müller-Caspary et al., 2017; Winkler et al., 2020), there is growing interest in quantitative structure determination approaches that handle dynamical diffraction, including neural networks (Van den Broek & Koch, 2012, 2013; Pennington et al., 2014), inverse multislice ptychography (Maiden et al., 2012; Schloz et al., 2020; Chen et al., 2021; Du et al., 2021; Bangun et al., 2022), tomography (Ren et al., 2020), and scattering-matrix-based inversion (Brown et al., 2018). However, not least because inverse problems can be subject to instabilities and are often time-consuming to solve, we think there is scope for less complex, qualitative analysis strategies—amongst other things, they could be used to initialize more complex algorithms.

One such strategy is the parallax method recently proposed by Ophus and coworkers (Ophus et al., 2019; Brown et al., 2022), which determines the so-called scattering matrix S (Sturkey, 1962) that maps the entrance-surface wave to the scattered exit-surface wave and uses it to synthesize a depth-sectioning phase series [similar to optical sectioning in Wigner distribution deconvolution ptychography (Yang et al., 2016)]. Because S can be reconstructed using 4D-STEM data from a small number of defocus values (Brown et al., 2018; Findlay et al., 2021; Pelz et al., 2021; Brown et al., 2022), this should be simpler experimentally than conventional depth sectioning via annular dark field

Received: November 24, 2022. Revised: March 15, 2023. Accepted: May 25, 2023

© The Author(s) 2023. Published by Oxford University Press on behalf of the Microscopy Society of America.

This is an Open Access article distributed under the terms of the Creative Commons Attribution License (<https://creativecommons.org/licenses/by/4.0/>), which permits unrestricted reuse, distribution, and reproduction in any medium, provided the original work is properly cited.

(ADF) (Borisevich et al., 2006) or DPC (Bosch & Lazić, 2019) where one must acquire individual images across many defocus values. Since the \mathcal{S} -matrix approach is a phase-contrast technique, it should also be sensitive to both light and heavy elements, unlike the strong atomic number dependence of ADF STEM.

This paper explores the depth resolution properties of the parallax phase reconstruction. We begin by deriving a mathematical equivalence between parallax reconstruction and a through-focal series acquired via confocal imaging with a hypothetical point-detector that can measure phase. We derive the contrast transfer function (CTF) and point spread function (PSF) for parallax imaging that are formally exact for weak objects, and analytically determine their resolution limits. We extend to thicker objects using doped Si as a case study to explore whether dynamical diffraction erodes the depth resolution found for weak objects. Using simulated 4D-STEM data, we test reconstruction accuracy in the presence of shot noise over three orders of magnitude in dose. We discuss challenges in making use of dark field information (i.e., signals originating from electrons scattered beyond the probe-forming semi-angle) to improve depth resolution. Lastly, we identify cases where the parallax reconstruction yields anomalous results.

Method

The Scattering Matrix

The scattering matrix \mathcal{S} was introduced into electron microscopy by Sturkey (1962). This operator maps the incident (entrance-surface) wavefunction ψ_{in} to the scattered (exit-surface) wavefield ψ_{out} as per

$$\psi_{\text{out}} = \mathcal{S}\psi_{\text{in}}. \quad (1)$$

Decomposing the wavefunction ψ_{in} and ψ_{out} into a series of plane waves indexed by transverse wavevectors \mathbf{g} and \mathbf{h} (the incident and scattered waves respectively), equation (1) can be expressed as

$$\psi_{\text{out}}(\mathbf{h}) = \sum_{\mathbf{g}} \mathcal{S}_{\mathbf{h},\mathbf{g}} \psi_{\text{in}}(\mathbf{g}). \quad (2)$$

Using the Fourier relation $\mathcal{S}_{\mathbf{r},\mathbf{g}} = \mathcal{F}_{\mathbf{h} \rightarrow \mathbf{r}}^{-1} \{ \mathcal{S}_{\mathbf{h},\mathbf{g}} \} = \sum_{\mathbf{h}} \mathcal{S}_{\mathbf{h},\mathbf{g}} e^{2\pi i \mathbf{h} \cdot \mathbf{r}}$, it is also possible to express this action in mixed real-space and Fourier-space such that

$$\psi_{\text{out}}(\mathbf{r}) = \sum_{\mathbf{g}} \mathcal{S}_{\mathbf{r},\mathbf{g}} \psi_{\text{in}}(\mathbf{g}), \quad (3)$$

with $\mathbf{r} = (r_x, r_y)$ the real-space coordinate in the sample plane.

Parallax Reconstruction

Consider the scattering system depicted in Figure 1a: a region of “thickness” t with a single atom-containing layer at depth z' from the top surface. The mixed real-space/Fourier-space \mathcal{S} -matrix for this system therefore consists of free-space propagation through distance z' , followed by a phase-object interaction with the (projected) scattering potential $V(\mathbf{r})$, followed by propagation through the remaining distance $t - z'$:

$$\mathcal{S}_{\mathbf{r},\mathbf{g}} = P_2(\mathbf{r}, t - z') \otimes_{\mathbf{r}} [e^{i\sigma V(\mathbf{r})} e^{-i\pi \lambda g^2 z'} e^{2\pi i \mathbf{g} \cdot \mathbf{r}}], \quad (4)$$

where $\otimes_{\mathbf{r}}$ denotes a convolution over \mathbf{r} , $e^{i\sigma V(\mathbf{r})}$ is the transmission function of the atomic layer (with interaction constant σ),

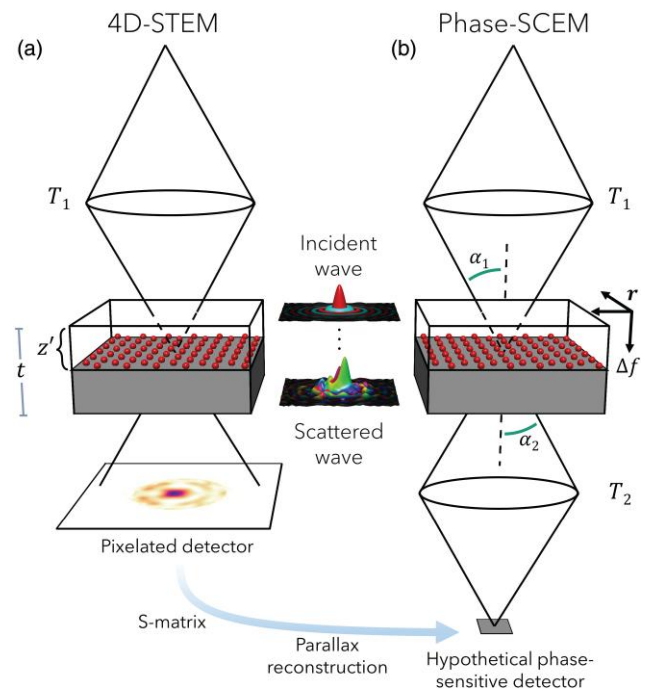


Fig. 1. Schematic illustrating the equivalence between (a) 4D-STEM followed by \mathcal{S} -matrix determination and parallax reconstruction and (b) scanning confocal electron microscopy (SCEM) with a (hypothetical) phase-sensitive point-detector. T_i denotes the transmission function of each lens, defined in terms of convergence semi-angle α_i .

λ denotes the (relativistically corrected) electron wavelength, and $P_2(\mathbf{r}, t - z') = \int A_2(\mathbf{k}') e^{-i\pi \lambda k'^2 (t - z')} e^{2\pi i \mathbf{k}' \cdot \mathbf{r}} d\mathbf{k}'$ is the Fresnel free-space propagator with a frequency cutoff effected by the aperture pupil function A_2 . This cutoff was not included in Brown et al. (2022), and is not explicitly part of the experimental setup in Figure 1a. However, in practice the detector extent is finite and there is a scattering angle beyond which the signal drops below either the level of shot noise or the contribution from thermal scattering [which is not described by equation (4)]. Consequently we may opt to only use information from a limited radial extent in Fourier space— A_2 allows for this. Note too that we will only be able to reconstruct $\mathcal{S}_{\mathbf{r},\mathbf{g}}$ for those \mathbf{g} which fall within the probe-forming aperture $A_1(\mathbf{g})$.

Following the derivation in Brown et al. (2022) (reproduced in Section 1 of the Supplementary Material), it can be shown that

$$\mathcal{S}_{\mathbf{r},\mathbf{g}} = e^{2\pi i \mathbf{g} \cdot \mathbf{r}} e^{-i\pi \lambda g^2 t} [P_{2,\mathbf{g}}(\mathbf{r}, t - z') \otimes_{\mathbf{r}} e^{i\sigma V(\mathbf{r} - \lambda(t - z')\mathbf{g})}], \quad (5)$$

with $P_{2,\mathbf{g}}(\mathbf{r}, z) = \int A(\mathbf{k}' + \mathbf{g}) e^{-i\pi \lambda z k'^2} e^{2\pi i \mathbf{k}' \cdot \mathbf{r}} d\mathbf{k}'$. This is equivalent to an \mathcal{S} -matrix where the sample potential has been translated some (lateral) distance $\lambda(t - z')\mathbf{g}$ before being propagated a distance $t - z'$, multiplied by additional phase factors.

Equation (5) is approximately invertible (see Section 2 of the Supplementary Material) such that from a measured \mathcal{S} we may estimate the transmission function of the sample via

$$e^{i\sigma V(\mathbf{r})} \approx \sum_{\mathbf{h},\mathbf{g}} e^{2\pi i \mathbf{h} \cdot \mathbf{r}} A_2(\mathbf{h}) e^{i\pi \lambda (t - z') h^2} \mathcal{S}_{\mathbf{h},\mathbf{g}} A_1(\mathbf{g}) e^{i\pi \lambda z' g^2} e^{-2\pi i \mathbf{g} \cdot \mathbf{r}}, \quad (6)$$

where the approximate equality reflects the fact that the fidelity of the reconstruction is reduced by the absence of the contributions from frequencies eliminated by either the

prespecimen aperture (A_1) or the postspecimen aperture (A_2).

Although derived assuming an object in a single plane z' , the parallax method proposes that the phase of the quantity on the right-hand side of equation (6) approximates the structure at any depth z and for any sample thickness. At best this can only be approximately true: even if different planes contribute independently (as per the undisturbed probe model of [Bosch & Lazić, 2019](#)) contributions from those multiple planes will be present in the parallax reconstruction at any given depth z . However, [Brown et al. \(2022\)](#) showed that the out-of-plane contributions are increasingly blurred out. Qualitatively then, we take the parallax reconstruction to approximate the sample potential subject to some elongation along the optical axis.

We can gain additional insight into equation (6) by a mathematical connection with scanning confocal electron microscopy (SCEM). Suppose we image a sample using a coupled set of pre- and postspecimen lenses, as in [Figure 1b](#), defined by the lens transfer functions $T_1(\mathbf{g}, \Delta f_1)$ and $T_2(\mathbf{h}, \Delta f_2)$. The wavefield in the image plane is then given by

$$\begin{aligned} \psi(\mathbf{r}, \Delta f_1, \Delta f_2) &= \sum_{\mathbf{h}, \mathbf{g}} e^{2\pi i \mathbf{h} \cdot \mathbf{r}} T_2(\mathbf{h}, \Delta f_2) \mathcal{S}_{\mathbf{h}, \mathbf{g}} T_1(\mathbf{g}, \Delta f_1) e^{-2\pi i \mathbf{g} \cdot \mathbf{r}} \\ \psi(\mathbf{r}, -z, -(t-z)) &= \sum_{\mathbf{h}, \mathbf{g}} e^{2\pi i \mathbf{h} \cdot \mathbf{r}} A_2(\mathbf{h}) e^{\pi i \lambda (t-z) b^2} \mathcal{S}_{\mathbf{h}, \mathbf{g}} A_1(\mathbf{g}) e^{\pi i \lambda z g^2} e^{-2\pi i \mathbf{g} \cdot \mathbf{r}}, \end{aligned} \quad (7)$$

where in the second line we have written the lens transfer functions in terms of their pupil functions ($A_1(\mathbf{g})$ and $A_2(\mathbf{h})$) and phase factors ($e^{-\pi i \lambda \Delta f_1 g^2}$ and $e^{-\pi i \lambda \Delta f_2 h^2}$), and enforced the confocal condition such that the two lenses are focused to the same depth z . We assume no other aberrations in the system besides defocus and adopt the convention that negative defocus indicates focusing into the sample.

The right-hand sides of equations (6) and (7) are identical, meaning that the result of the (ideal, up to the cutoff frequency implied by A_2) parallax reconstruction is the same as that of the [Figure 1b](#) setup of SCEM paired with a hypothetical point detector that directly measures phase. We refer to the latter as phase-SCEM. Although not achievable experimentally, this conceptual framework will aid our exploration of the resolution properties of the parallax reconstruction.

Results

Analytic Treatment for Weak Objects

Following previous work ([Cosgriff et al., 2008](#); [D'Alfonso et al., 2008](#); [Xin & Muller, 2009](#); [Bosch & Lazić, 2019](#)), we can analytically establish the resolution properties of phase-SCEM, and in turn that of the parallax method for a weak object, by deriving PSF-like and CTF-like quantities. We stress at the outset that phase-SCEM is an idealization, in particular because it is unclear what noise properties could be attributed to a hypothetical phase-sensitive point-detector. Effective CTFs can be defined for iterative reconstruction algorithms ([Zhou et al., 2020](#); [O'Leary et al., 2021](#)), an approach that could be adapted for scattering matrix determination. However, given our goal of exploring the depth resolution properties, in the present section we consider the noise-free idealization to give a concrete, best-case-scenario baseline. We return to the question of the limitations due to noise in a later section.

Substituting the reciprocal space form of equation (4) into equation (7) yields

$$\psi(\mathbf{r}, z) = [e^{i\sigma V(\mathbf{r})} \delta(z-z')] \otimes_{(\mathbf{r}, z)} [P_1(-\mathbf{r}, -z) P_2^*(-\mathbf{r}, -z)], \quad (8)$$

where $P_i(\mathbf{r}, z) = \sum_{\mathbf{g}} A_i(\mathbf{g}) e^{-\pi i \lambda z g^2} e^{2\pi i \mathbf{g} \cdot \mathbf{r}}$ defines the wavefield for a STEM probe with some aperture function A_i (defined in terms of convergence semi-angle α_i , as per [Fig. 1](#)), reconstruction depth z , and free of any other aberrations. Note that equation (8) is essentially equation (9) of [Cosgriff et al. \(2008\)](#).

Under the weak phase object approximation (WPOA) $e^{i\sigma V(\mathbf{r})} = 1 + i\sigma V(\mathbf{r})$, equation (8) becomes ([Section 3 in the Supplementary Material](#))

$$\psi^{\text{WPOA}}(\mathbf{r}, z) = 1 + i\sigma [V(\mathbf{r}) \delta(z-z')] \otimes_{(\mathbf{r}, z)} [P_1(-\mathbf{r}, -z) P_2^*(-\mathbf{r}, -z)]. \quad (9)$$

For $\alpha_1 = \alpha_2$, $P_1(-\mathbf{r}, -z) P_2^*(-\mathbf{r}, -z) = |P_1(-\mathbf{r}, -z)|^2$ is real and the intensity of $\psi^{\text{WPOA}}(\mathbf{r}, z)$ only has a second-order term in $V(\mathbf{r})$. This was previously shown by [Cosgriff et al. \(2008\)](#), and explains why the phase contrast of weak phase objects in coherent SCEM imaging is very weak. However, the phase of ψ^{WPOA} is given by

$$\phi^{\text{WPOA}}(\mathbf{r}, z) = \sigma [V(\mathbf{r}) \delta(z-z')] \otimes_{(\mathbf{r}, z)} |P_1(-\mathbf{r}, -z)|^2. \quad (10)$$

The form of equation (10) is strongly reminiscent of a linear imaging model: the object $\sigma V(\mathbf{r}) \delta(z-z')$ is convolved by a PSF-like $|P_1(-\mathbf{r}, -z)|^2$ to yield the measured quantity $\phi^{\text{WPOA}}(\mathbf{r}, z)$. In the idealization of phase-SCEM, by hypothesis the phase is indeed the measured quantity. In practice, the phase in equation (10) [or the wavefunction in equation (9)] would need first to be obtained, which we do in later sections via an iterative algorithm. To emphasize this indirectness, that any limitations of that precursor step are not conveyed by equation (10), we will refer to the relevant quantities as pseudo-PSFs. Equation (10) shows the pseudo-PSF of phase-SCEM to be proportional to the 3D probe intensity, which is also true of the PSF of depth sectioning for ADF ([D'Alfonso et al., 2008](#); [Xin & Muller, 2009](#)) and DPC ([Bosch & Lazić, 2019](#)), meaning that the resolution limits of weak objects in an idealized, noise-free parallax reconstruction with $\alpha_1 = \alpha_2$ is identical to that of these imaging modes.¹

For $\alpha_2 > \alpha_1$, the product $P_1(-\mathbf{r}, -z) P_2^*(-\mathbf{r}, -z)$ is not purely real (for $z \neq 0$). Then, to first order in $V(\mathbf{r})$,

$$\phi^{\text{WPOA}}(\mathbf{r}, z) = \sigma [V(\mathbf{r}) \delta(z-z')] \otimes_{(\mathbf{r}, z)} \Re [P_1(-\mathbf{r}, -z) P_2^*(-\mathbf{r}, -z)] \quad (11)$$

and the pseudo-PSF is proportional to $\Re [P_1(-\mathbf{r}, -z) P_2^*(-\mathbf{r}, -z)]$. When $\alpha_2 > \alpha_1$, we expect P_2 to have better resolution than P_1 , and therefore phase-SCEM and/or the parallax reconstruction to have better depth sensitivity than that of depth-sectioning incoherent STEM defined by the same probe-forming aperture α_1 .

¹ Ptychography may also be used to effect a form of synthesized optical sectioning ([Yang et al., 2016](#)), with contrast transfer limits identical to the aforementioned techniques, though the PSFs/CTFs in ptychography are different in detail, as most evident in the WPOA case comparing ptychography and DPC ([Pennycook et al., 2015](#)).

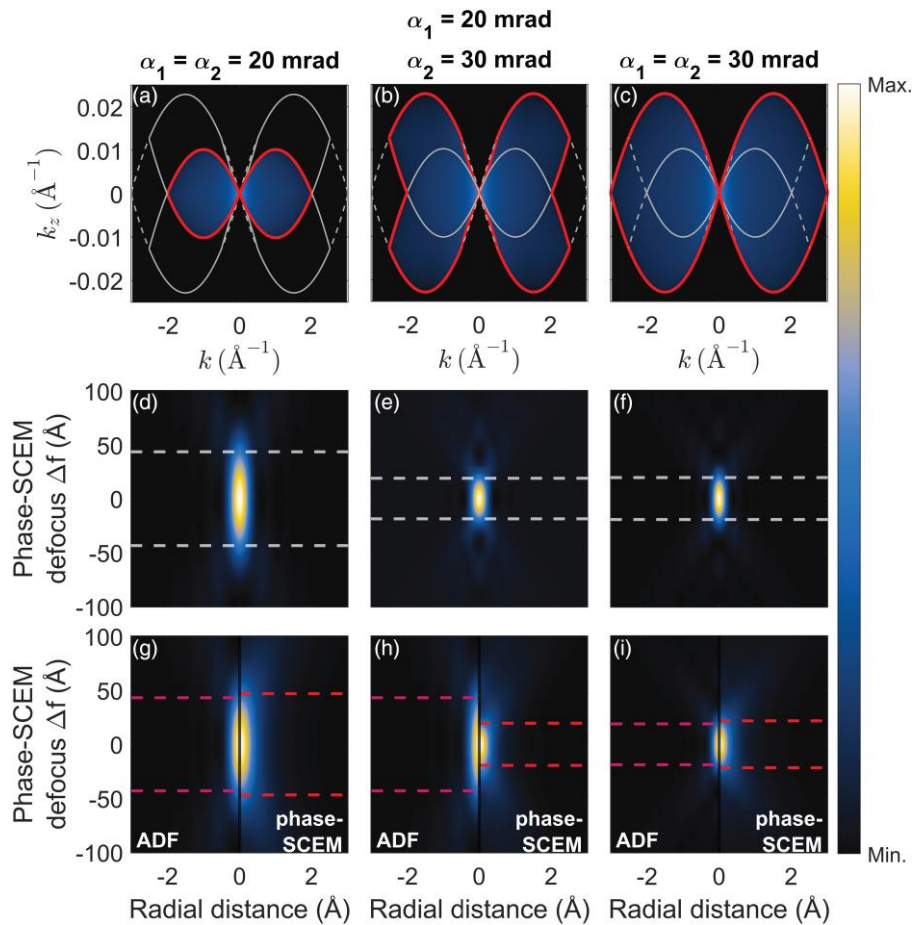


Fig. 2. (a)–(c): Analytically calculated pseudo-CTFs for phase-STEM, plotted on a cube-root amplitude scale to enhance the visibility of smaller values. The analytic boundaries are overlaid as bold curves for each particular α_1, α_2 pair. Narrow curves show for comparison the limits associated with the other convergence semi-angles. (d)–(f): Analytically computed pseudo-PSFs for phase-STEM. Overlaid dotted lines indicate the FWHM of each probe. (g)–(i): ADF STEM and phase-STEM simulations of a single isolated Bi atom. The ADF detector extends from 60 to 160 mrad, and the dotted lines again denote the FWHM of each peak. All calculations assume 300 keV electrons.

By definition, the pseudo-CTF is the Fourier transform of the pseudo-PSF:

$$\begin{aligned} \text{pseudo-CTF}_\phi(\mathbf{k}, k_z) \\ = \int \Re[P_1(-\mathbf{r}, -z)P_2^*(-\mathbf{r}, -z)] e^{-2\pi i \mathbf{k} \cdot \mathbf{r}} e^{-2\pi i k_z z} d\mathbf{r} dz, \end{aligned} \quad (12)$$

where $\mathbf{k} = (k_x, k_y)$. It can be shown (Section 4 of the Supplementary Material) that nonzero information transfer only occurs for

$$|k_z| < \min \left[k\alpha_1 + \lambda \frac{k^2}{2}, k\alpha_2 - \lambda \frac{k^2}{2} \right], \quad (13)$$

with $k = |\mathbf{k}|$. Additionally, if $2(\alpha_1/\lambda) \leq k \leq (\alpha_1 + \alpha_2)/\lambda$, $|k_z| > |k\alpha_1 - \lambda(k^2/2)|$.

The top row of Figure 2 shows the pseudo-CTFs for three different aperture combinations, with the analytic bounds of equation (13) overlaid in red for a 300 keV accelerating voltage. The $\alpha_1 = \alpha_2 = 20$ mrad case in Figure 2a and the $\alpha_1 = \alpha_2 = 30$ mrad case in Figure 2c have the “propeller” shape previously shown for incoherent STEM imaging (D’Alfonso et al., 2008; Xin & Muller, 2009), including the “missing wedge” of effective tilt angles² for small k and an

increasing lateral and vertical extent for larger α . Note that the nonzero transfer at $\mathbf{k} = 0$ is nonphysical, a consequence of our artificial assumption of a phase-sensitive point-detector, whereas in practice we could at best hope to measure relative phase differences. We stress again that the detailed values of the pseudo-CTF are only relevant to the idealized, noise-free limit, and as such we focus here on the resolution limits that govern the maximum depth resolution possible in this imaging mode. As per ADF and DPC depth sectioning, one route to improving depth resolution for phase-STEM and parallax reconstruction is to increase the probe-forming aperture angle α_1 . However, Figure 2b shows an alternative: the $\alpha_1 = 20$ mrad and $\alpha_2 = 30$ mrad pseudo-CTF has the same vertical

² Since the opening angles of the pseudo-CTFs at low spatial frequencies match the tens-of-milliradian convergence semi-angles of the probe, this depth-sectioning technique can be likened to traditional tilt tomography with a tilt angle defined by the probe convergence semi-angle. The “missing wedge” of effective tilt angles causes distortions in conventional tilt-series tomography (Frank, 1992). For certain classes of specimen, *a priori* knowledge about the specimen can significantly suppress missing wedge artifacts, for example using discrete tomography algorithms (Bals et al., 2009). In multislice ptychography, sparsity constraints of crystalline atomic positions have similarly been used to regularize the structure determination (Schloz et al., 2020). We do not employ any such strategies here and so elongation distortions manifest in the PSFs in Figure 2.

extent as the $\alpha_1 = \alpha_2 = 30$ mrad pseudo-CTF (though slightly narrower lateral extent). Thus the depth resolution of phase-SCEM and parallax reconstructions can in principle be increased for fixed α_1 by increasing α_2 , i.e. using signal in the dark-field region.

The middle row of Figure 2 shows the pseudo-PSFs for phase-SCEM following equations (10) and (11), with dashed lines indicating the full-width at half-maximum (FWHM). Consistent with our discussion of the pseudo-CTFs, the pseudo-PSFs are more localized along the defocus direction for $\alpha_2 = 30$ mrad, whether $\alpha_1 = 30$ mrad (Fig. 2f) or $\alpha_1 = 20$ mrad (Fig. 2e).

The bottom row of Figure 2 shows through-focal ADF STEM and phase-SCEM simulations for a single, isolated Bi atom, also at 300 keV. Although Bi is not necessarily a weak scatterer, the extent of these depth-sectioning simulations closely matches that of the pseudo-PSFs in the middle row of Figure 2. Figure 2g shows good agreement between ADF STEM depth sectioning for $\alpha_1 = 20$ mrad and phase-SCEM for $\alpha_1 = \alpha_2 = 20$ mrad, the ADF signal being marginally narrower because the object function for thermal scattering is narrower than that for elastic scattering. Figure 2i shows similarly good agreement between ADF STEM depth sectioning for $\alpha_1 = 30$ mrad and phase-SCEM for $\alpha_1 = \alpha_2 = 30$ mrad. Figure 2h reinforces the potential advantages of phase-SCEM and, by extension, parallax phase reconstruction: by extending the postspecimen aperture collection semi-angle α_2 beyond that of α_1 , the depth resolution is improved comparably to increasing α_1 . If achievable in practice (we discuss later some impediments due to noise and thermal diffuse scattering), this could either reduce the need for careful aberration tuning to increase resolution by opening the prespecimen aperture or else allow a reduced dose rate through decreased aperture size without sacrificing resolution.

In the noise-free idealization, the pseudo-CTF/pseudo-PSF formulation yields analytic results for weak objects, but the WPOA breaks down for thicker samples, where dynamical diffraction occurs. Since the depth resolution of a single atom is much broader than the interatomic spacing, we explore how the presence of multiple atoms impacts depth resolution in phase-SCEM and the parallax reconstruction by considering substitutional dopants in a supporting crystal matrix.

Idealized, Noise-Free Calculations for a Thick Crystal

We choose our reference crystal to be Si, a well-known sample in electron microscopy and one which underpins modern microelectronics. Oriented along a [001] zone axis, we simulate both heavy and light substitutional dopants. The specific choice of dopants—Bi, As, N, and B—is motivated by common additives in Si-based semiconductors (Fahey et al., 1989) also used in early ADF depth-sectioning studies (Borisevich et al., 2006; Voyles, 2006; Cosgriff & Nellist, 2007; Oshima et al., 2010). We consider a range of atomic species to explore how dopant resolvability might depend on atomic number. In this section, we again use the noise-free idealization of phase-SCEM, before turning our attention to limitations due to noise in the next section.

Our method for assessing depth resolution of dopants in Si is as follows. From absorptive multislice phase-SCEM simulations³ (for an aberration-free probe with perfect coherence and an accelerating voltage of 300 keV), Figure 3 shows a

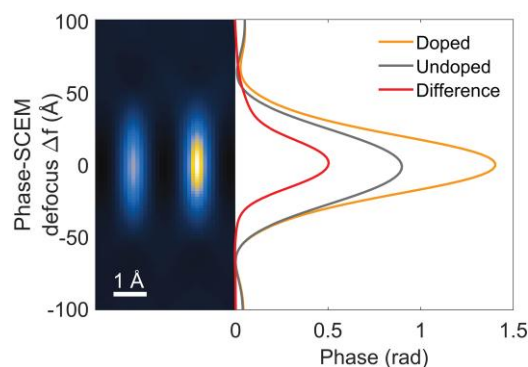


Fig. 3. Left: Multislice-calculated phase-SCEM imaging for a 49 Å thick Bi-doped Si sample using convergence semi-angles $\alpha_1 = \alpha_2 = 30$ mrad, with a doped and an undoped column in the field-of-view. The sample was oriented along the [001] zone axis, with the horizontal direction being [110]. Right: Line profiles taken vertically (i.e., as a function of defocus) through the centers of each of the doped and undoped columns, as well as the difference between the two. The difference signal is taken as representative of the scattering contribution from the Bi dopant atom.

2D cross-section—along the [110] direction laterally and the [001] direction in defocus—that encompasses both Bi-doped (brighter) and undoped (fainter) columns. We take through-focus line profiles along the centers of each column. We then construct a difference signal between the doped column and a pure Si reference. When dynamical diffraction occurs, this signal is not strictly attributable solely to the dopant, though this would be true in the undisturbed probe model of Bosch & Lazić (2019). Pragmatically nonetheless, we will assess dopant visibility and the depth resolution properties of phase-SCEM in thick samples based on this difference signal.

Figure 4 explores how the depth resolution of an isolated atom compares to difference signals for various thicknesses, convergence semi-angle pairs, dopant species and dopant depths (results exploring further parameter combinations are given in Section 5 of the Supplementary Material). The colored lines correspond to different crystal thicknesses, ranging from 27 to 179 Å, while the thick black lines correspond to an isolated atom. Minor, nonmonotonic fluctuations can be seen as a function of thickness (i.e., between the various colored lines), a result of the oscillating nature of electron channeling along the column (Wu et al., 2017). Nevertheless, the width of the profiles is similar to that of the isolated atoms for all thicknesses considered: dynamical diffraction does not significantly alter the resolvability of individual dopants.

The top row in Figure 4 explores various convergence semi-angle combinations for a Bi dopant located in the sample mid-layer. Both $\alpha_2 = 30$ mrad cases have higher depth resolution (narrower profiles) than the $\alpha_2 = 20$ mrad case. In the $\alpha_1 = 20$ mrad and $\alpha_2 = 30$ mrad case, the asymmetry between the apertures results in some asymmetry in the profile with depth.

The middle row of Figure 4 explores the influence of atomic number, with $\alpha_1 = \alpha_2 = 20$ mrad and dopants located in the sample mid-layer. The depth resolution is essentially the same for all dopant species, though the contrast in the

³ Accounting for thermal diffuse scattering via the absorptive model allows for an unambiguous coherent, elastic scattering wavefield, as implicitly assumed in the phase-SCEM formulation in equation (7). It is unclear whether the phase-SCEM idealization could usefully be generalized to handle incoherence from the positive contribution of thermally scattered electrons. We instead return to it later as a limitation of practice for the parallax reconstruction.

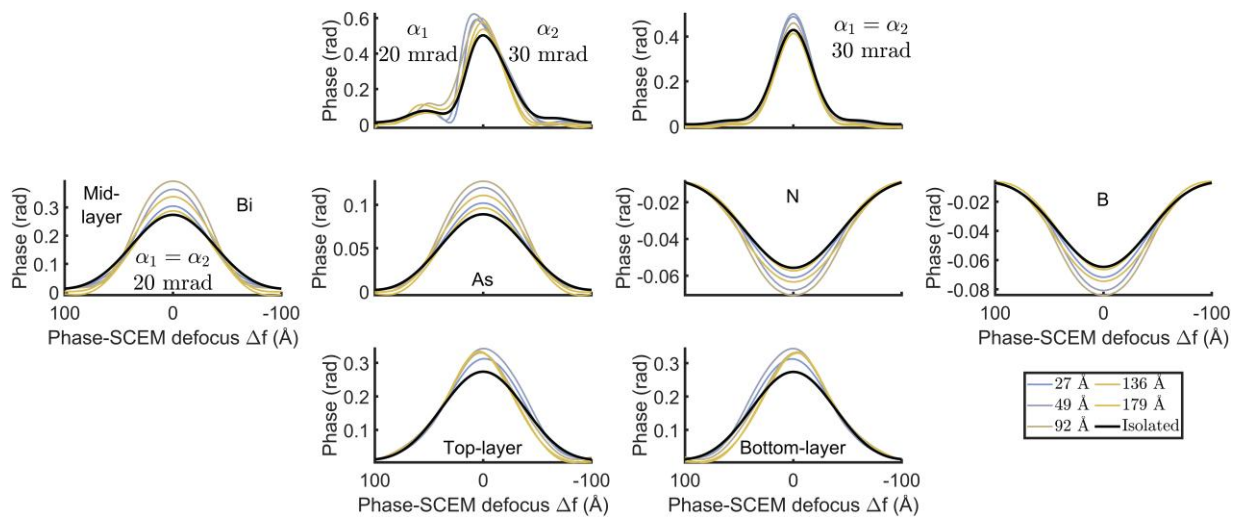


Fig. 4. Scattering signals from individual dopant atoms taken as the difference between phase-SCEM defocus profiles from doped and undoped columns for a range of configurations. Top row: Phase-SCEM signal from a Bi dopant located at the sample mid-plane for select convergence semi-angle combinations. Middle row: Phase-SCEM signals for various dopants placed at the sample mid-plane, assuming $\alpha_1 = \alpha_2 = 20$ mrad. Bottom row: Phase-SCEM signals from a Bi dopant for various depths along the atomic column, assuming $\alpha_1 = \alpha_2 = 20$ mrad. In all cases the defocus scale is referenced to the dopant depth. The colored lines indicate the dopant signals from crystals of different thickness (from 27 to 179 Å), and overlaid in black are the difference signals between isolated dopant and Si atoms under the same imaging parameters. All calculations assume 300 keV electrons.

difference signal reverses for dopants lighter than Si. The phase range of the profiles varies with atomic species, roughly proportional to the difference in atomic number between each dopant and the underlying Si. In these ideal simulations, the dopants are all detectable across all thicknesses.

The bottom row in Figure 4 explores various dopant depths, assuming a Bi dopant and $\alpha_1 = \alpha_2 = 20$ mrad. Whereas the center dopant case on the far left results in a fairly symmetric profile, having the dopant on the bottom or the top introduces minor asymmetry in the line profiles, but the depth resolution remains largely unchanged. In particular, the results in Figure 4 do not show the interpretive ambiguities due to channeling that have been reported for ADF (Xin et al., 2008). However, silicon is a relatively weak scatterer, and in a later section we show some interpretive challenges that can arise in more strongly scattering samples.

These results clearly show that the depth resolution of phase-SCEM for substitutional dopants is not much affected by a modest amount of dynamical diffraction from the supporting matrix. However, we are ultimately interested in parallax phase reconstruction of the \mathcal{S} -matrix from experimental data. We therefore explore how inaccuracies in \mathcal{S} -matrix determination impact the depth resolution and sensitivity of the parallax method.

Noise-Limited Calculations for a Thick Crystal

Realizing parallax phase reconstruction from simulated, noisy 4D-STEM can be described in three steps.

First, we use absorptive multislice calculations to simulate \mathcal{S} -matrices for the different dopants and crystal thicknesses at 300 keV. 4D-STEM images are evaluated according to

$$I(\mathbf{h}, \mathbf{r}, \Delta f) = \left| \sum_{\mathbf{g}} \mathcal{S}_{\mathbf{h},\mathbf{g}} T(\mathbf{g}, \Delta f) e^{-2\pi i \mathbf{g} \cdot \mathbf{r}} \right|^2. \quad (14)$$

Shot noise is introduced following a Poisson distribution based on the intensity at each point in the diffraction pattern.

Second, though other \mathcal{S} -matrix reconstruction approaches (Brown et al., 2018; Pelz et al., 2021; Brown et al., 2022) could be used, we carry out \mathcal{S} -matrix reconstruction via the phase retrieval process described in Findlay et al. (2021) with the following minor modifications. The method was extended to handle 4D-STEM data from multiple defocus values. We use 2D Savitzky-Golay filtering (Savitzky & Golay, 1964) rather than total generalized variation for smoothing as a form of regularization. We do not enforce antidiagonal symmetry, which, given the initialization of the phase retrieval, has the effect of subsuming the thickness factor from equation (7) into the reconstructed \mathcal{S} -matrix (i.e., $\mathcal{S}_{\mathbf{h},\mathbf{g}}^{\text{recon}} \approx e^{i\pi \lambda t^2} \mathcal{S}_{\mathbf{h},\mathbf{g}}^{\text{true}}$). This is fortunate because now the thickness need not be known, leaving the expression defined purely in terms of the reconstruction depth z .

Finally, the reconstructed \mathcal{S} -matrix is substituted into equation (7), taking the phase of which yields a signal which should nominally be identical to our hypothetical phase-SCEM setup. In contrast to our discussion of phase-SCEM, where defocus represented the coordinate along the optical axis, in equation (14) Δf denotes the probe defocus used to form the 4D-STEM image(s). As per the parallax reconstruction of equation (7), we will hereafter refer to the coordinate along the optical axis as the reconstruction plane z .

As before, the difference between depth profiles through a doped and undoped reference Si column is taken to reflect the scattering contribution solely from the dopant. We present the results of these reconstructions only for a Bi dopant embedded in the sample mid-plane. Nonetheless, the trends we observe and conclusions we draw apply equally to the other dopant species and locations.

Bright-Field Reconstructions

Beginning with $\alpha_1 = \alpha_2 = 20$ mrad, i.e. operating solely in the bright field, we simulate 4D-STEM data for Bi-doped Si crystals with thicknesses of 27, 92, and 179 Å. The aberration-free probe is focused at the depth of the dopant, the sample mid-plane, on the assumption that this maximizes the interaction

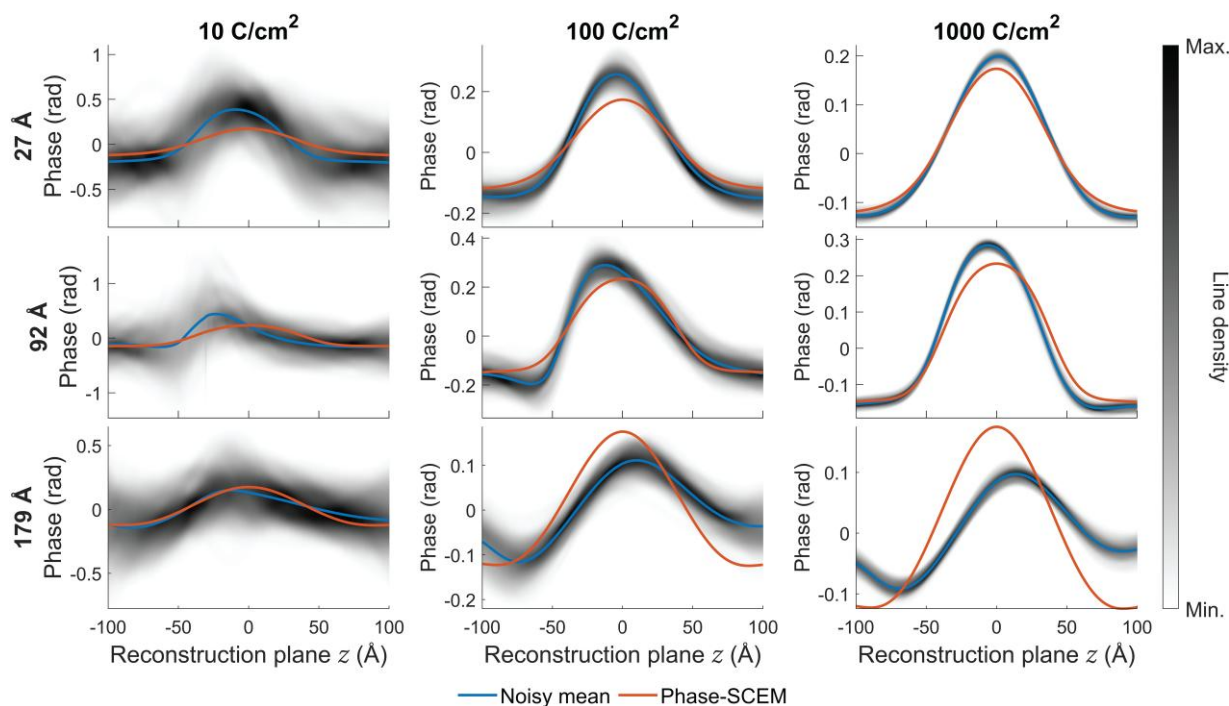


Fig. 5. Difference signal line profiles from noisy \mathcal{S} -matrix parallax reconstruction with $\alpha_1 = \alpha_2 = 20$ mrad and 300 keV electrons. The sample was Si, with the Bi dopant placed in the sample mid-layer and the probe focused on the mid-layer. Results are shown for three different dose levels (columns) and thicknesses (rows). Profiles for 100 noise realizations are shown using shading to denote line density. The mean for each noisy dataset and the signal from ideal (noise-free) phase-SCEM are overlaid on each plot.

between the electron beam and the dopant. The probe scan across the specimen is sampled at 0.226 \AA per pixel, just above the Nyquist-Shannon sampling frequency. Each diffraction pattern has a Fourier-space sampling of 0.59 mrad per pixel. We consider doses spanning three orders of magnitude: a low dose of 10 C/cm^2 ($\sim 6,200 \text{ e}^-/\text{\AA}^2$), a high dose of 100 C/cm^2 ($\sim 62,000 \text{ e}^-/\text{\AA}^2$), and a very high dose of $1,000 \text{ C/cm}^2$ ($\sim 620,000 \text{ e}^-/\text{\AA}^2$) (Yang et al., 2015). We simulate 100 distinct noise realizations at each dose level and thickness to explore the statistical variation in the parallax reconstructions due to noise. Figure 5 summarizes these results, visualizing the different noise realizations as a shaded line density distribution calculated via kernel density estimation. Increasing the incident dose results in a more compact distribution as the variation due to noise becomes less severe.

For low dose, while many noise realizations for thinner samples would be suggestive of the presence of a dopant, the signal variability with noise is comparable to the signal of the Bi dopant, and so the Bi dopant would not be unambiguously visible above noise. However, the Bi dopant is clearly visible in the high and very high dose cases. Figure 5 only shows results for the Bi dopant. The visibility of the lighter dopants considered in Figure 4 can be gauged by comparing their phase range with the variation with noise in Figure 5. An As dopant would be barely detectable above noise in the high dose case, since its phase range of about 0.1 mrad is comparable to the noise variation at that dose. However, both As and B dopants should be visible at very high dose.

In Figure 5, the mean of the noise realizations distribution is plotted in blue, and the noise-free phase-SCEM results in orange. Because phase is only defined up to an arbitrary additive constant, we subtract the average phase of each line profile to allow for a meaningful comparison. For thicknesses of 27 and 92 \AA , there is generally good agreement between the means of

the noisy data and the ideal phase-SCEM result. However, for the 179 \AA profiles, although the increased dose still suppresses the variance due to noise, the mean of the noisy data is appreciably different from the phase-SCEM result. This proves to be a limitation of the phase retrieval: parallax reconstructions based on \mathcal{S} -matrix determination via phase retrieval on noise-free simulated data are closer to the mean of the noisy data than to the ideal phase-SCEM result, unless much fine-tuning of the phase retrieval hyperparameters is undertaken. The implication is that for the 179 \AA thick case the different noise realizations limit the accuracy of the \mathcal{S} -matrix determination in a way which systematically impacts the parallax reconstruction.

This limited accuracy of \mathcal{S} -matrix determination was more acute for $\alpha_1 = \alpha_2 = 30$ mrad, which is perhaps unsurprising since increasing the aperture size increases the number of unknowns to solve for. To ameliorate this, for $\alpha_1 = \alpha_2 = 30$ mrad we used two 4D-STEM datasets taken at a defocus of 20 \AA either side of the dopant plane. To keep the total dose incident on the sample constant, we utilize dose fractionation across the two defocus datasets. The results are shown in Figure 6, where we again compare 100 noise realizations (and their mean, in blue) against ideal phase-SCEM simulations (orange) on a common scale after having subtracted their respective means. Using two defocus values appears effective at improving the agreement between the mean of the noisy data and the phase-SCEM results, though some differences remain, most notably at the 100 C/cm^2 dose.

Comparing the $\alpha_1 = \alpha_2 = 30$ mrad results in Figure 6 with the $\alpha_1 = \alpha_2 = 20$ mrad results in Figure 5, we see that the variation with noise is larger in the 30 mrad case for the low and high doses, with more fluctuations in the profile: given the same overall dose, the increased difficulty of the phase retrievals due to the increased number of unknown \mathcal{S} -matrix

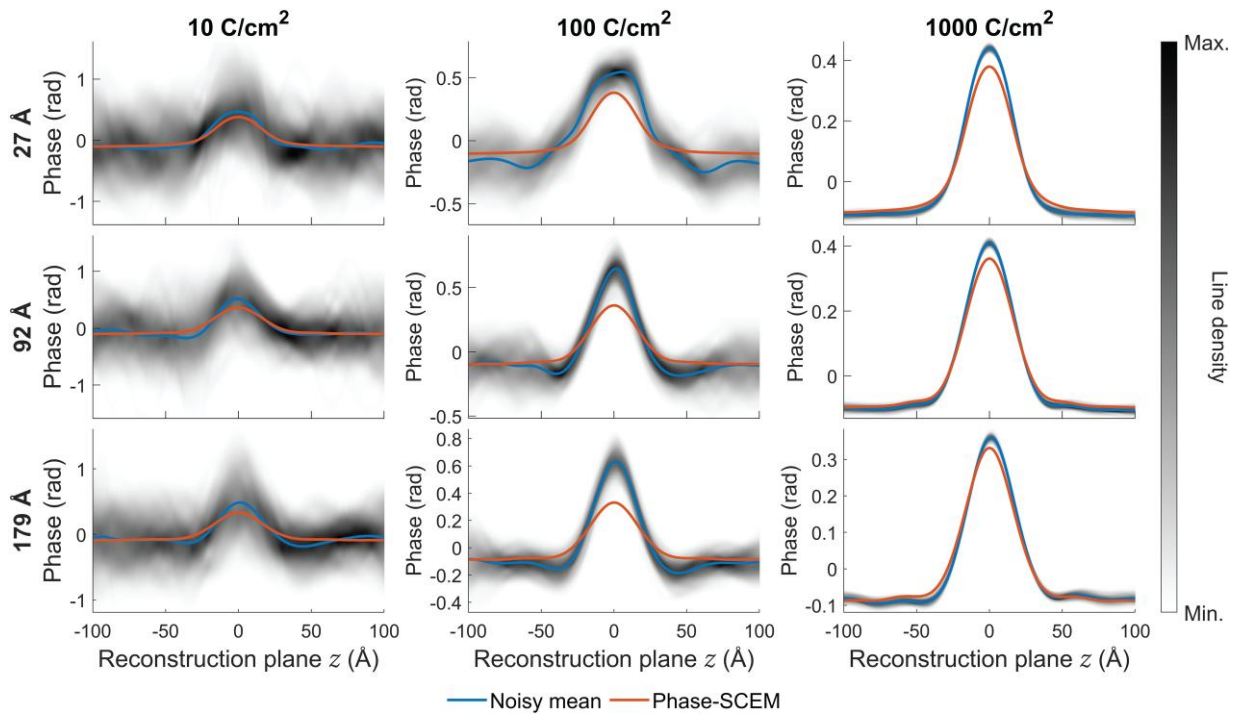


Fig. 6. Difference line profiles from noisy S -matrix parallax phase reconstruction with $\alpha_1 = \alpha_2 = 30$ mrad and 300 keV electrons. The sample was Si, with the Bi dopant placed in the sample mid-layer, and 4D-STEM data sets generated for defoci of 20 Å above and below the dopant plane. Results are shown for three different dose levels (columns) and thicknesses (rows). Profiles for 100 noise realizations are shown using shading to denote line density. The mean for each noisy dataset and the signal from ideal (noise-free) phase-SCEM are overlaid on each plot.

elements to be determined is not overcome by having 4D-STEM data from two defocus values. However, the converse is true at very high dose, producing parallax reconstruction with less noise variation in the $\alpha_1 = \alpha_2 = 30$ mrad case than in the $\alpha_1 = \alpha_2 = 20$ mrad case. In principle, the results can be further improved by increasing the separation between the defocus values of the 4D-STEM datasets, providing a greater diversity of scattering information. However, our results should be regarded as a best-case scenario since they assume perfect alignment between the datasets for different defocus values. In practice, misalignment would reduce the reliability of the phase retrievals, and alignment is likely more difficult the larger the defocus separation.

We have not applied any preprocessing to denoise the simulated 4D-STEM data, being more interested in how limitations on the accuracy of S -matrix determination due to noise affect the depth resolution and dopant visibility. We therefore expect these results to be a pessimistic estimate of the impact of noise on the visibility of dopants for the given dose values, since denoising strategies (Zhang et al., 2020) would likely improve the parallax reconstructions.

The discussion above focuses on the visibility of the dopant contribution above a signal variability due to noise in the parallax reconstruction. While different noise realizations affect the range and smoothness of the difference profile, the visual impression from Figures 5 and 6 is that if the dopant is visible in the presence of noise then its depth resolution is similar to the ideal, isolated atom result. In simulated inverse multislice ptychography reconstructions, Chen et al. (2021) show that there is a clear trend towards higher depth resolution of dopants as dose increases. Simple quantitative measures of the depth resolution in Figures 5 and 6 do not show any such clear trend. We think this is another consequence of how noise

limits the phase retrievals that determine the S -matrix in ways that we have not yet found a way to predict. Further work is needed to determine whether this could be overcome by refining the phase retrieval step, or whether it requires the additional “regularization” of the inverse multislice ptychography method’s constraint that the 4D-STEM intensities result from a multislice solution to the Schrödinger equation.

Another factor that could impact the parallax reconstruction is thermal diffuse scattering, since the incoherent contribution of such electrons to the 4D-STEM intensities introduces an inconsistency in the phase retrieval problem used to determine the scattering matrix. However, as shown in the Supplementary Figure S5, for the present Si case study the impact of thermal diffuse scattering is minimal, certainly less than the limitations on phase retrieval discussed above.

Dark-Field Reconstructions

The resolution limits for weak objects and the phase-SCEM simulations presented earlier demonstrate greater resolution by leveraging information beyond the bright field disk. However, there is an impediment to using signal in the dark field due to a subtlety in S -matrix determination. In equation (14), there is an ambiguity such that if $S_{\mathbf{h},\mathbf{g}}$ is a solution of the phase retrieval problem then so too is $e^{i\phi_{\mathbf{h}}} S_{\mathbf{h},\mathbf{g}}$ for arbitrary (real) values $\phi_{\mathbf{h}}$. For \mathbf{h} in the bright field region, this is partly overcome by the implicit phase relation established by the phase retrieval initialization of $S_{\mathbf{h},\mathbf{g}} = \delta_{\mathbf{h},\mathbf{g}}$ (Findlay et al., 2021). In the dark field however, we are unable to initialize the rows \mathbf{h} in the S -matrix the same way: the probe-forming aperture $A_1(\mathbf{g})$ means that the element $\mathbf{g} = \mathbf{h}$ for \mathbf{h} in the dark field region does not contribute to the 4D-STEM signal. Thus, even if the phase retrievals for individual rows \mathbf{h} in the S -matrix converge when \mathbf{h} is in the dark field, those dark field

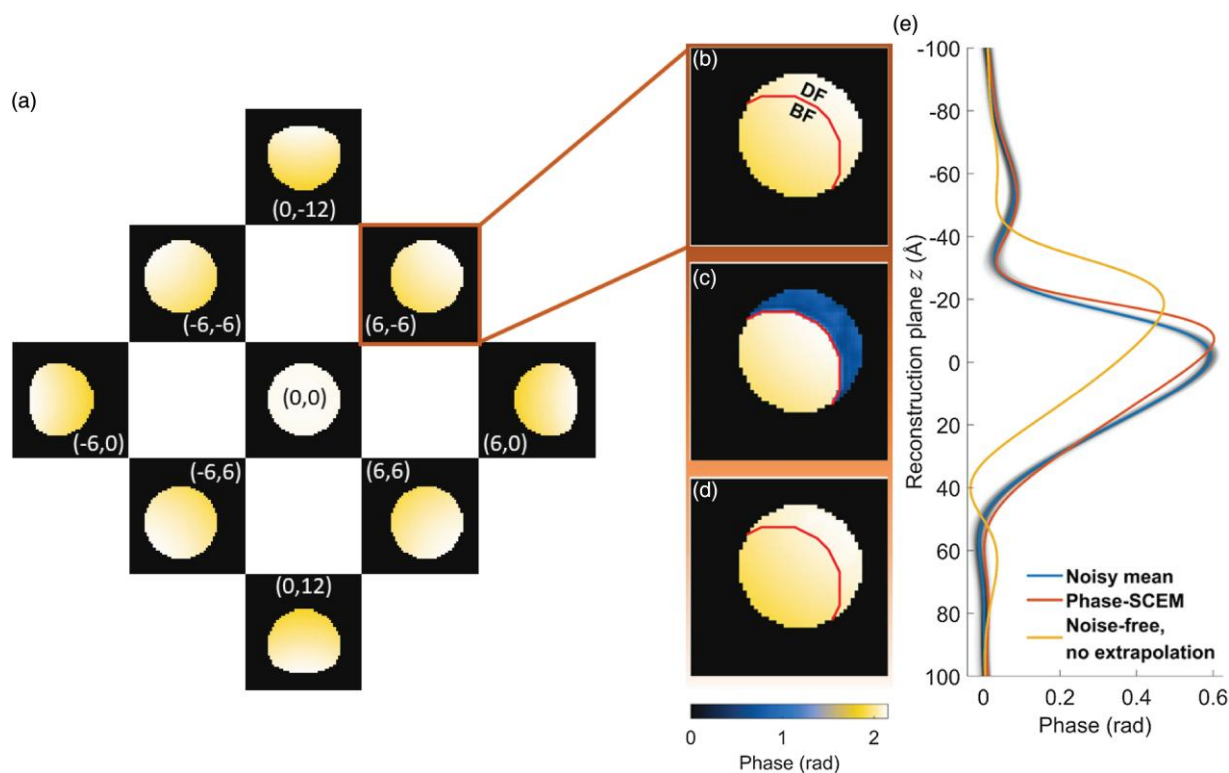


Fig. 7. (a) Visualization of the phase of the S -matrix, displayed as a mosaic where each tile corresponds to a different \mathbf{G} vector (expressed in integer multiples of reciprocal space lattice vectors for the 3×3 Si supercell) and shows $S_{\mathbf{h}+\mathbf{G},\mathbf{h}}$ as a function of “coordinate” \mathbf{h} , from a 27 Å Bi-doped Si crystal. For $\mathbf{G} = (6, -6)$, we show (b) the multislice-calculated S -matrix, (c) a reconstructed S -matrix with no phase pinning between the bright- and dark-field regions, and (d) a reconstructed S -matrix where polynomial fitting was used to extrapolate the converged bright field results into the dark field region to re-initialize the phase retrieval. The bright-field (labelled BF) and dark-field (labelled DF) regions are demarcated by a line. (e) Parallax reconstruction difference profile for 100 different noise realizations using extrapolated results from the bright field, on which is overlaid the mean, the corresponding phase-SCEM calculation, and a dark-field parallax reconstruction from an instance of noise-free phase retrieval without the modified initialization.

rows will not necessarily be phased correctly relative to the bright field region or to one another.

We illustrate this in Figure 7, with the S -matrix of 27 Å thick Bi-doped Si. Figure 7a visualizes the phase of portions of the S -matrix, specifically that of $S_{\mathbf{h}+\mathbf{G},\mathbf{h}}$ as images over “coordinate” \mathbf{h} for select \mathbf{G} expressed in integer multiples of reciprocal space lattice vectors for the 3×3 Si supercell used in our dopant simulations (see Findlay et al., 2021 for more detail on this visualization strategy). Figure 7b focuses specifically on $\mathbf{G} = (6, -6)$. Assuming $\alpha_1 = 20$ mrad, the dividing line between S -matrix elements which contribute to the bright-field region and to the dark-field region is indicated. The bright-field/dark-field division is a property of the imaging, not of the S -matrix itself, and the phase is seen to be both smooth and continuous across both regions.

Figure 7c shows the result from phase retrieval when nothing particular is done to pin the phases in the dark field region: while each of the two regions is self-consistent, we see a clear phase offset between the dark field and bright field regions. Figure 7e shows the impact this has on the parallax reconstruction difference profile: relative to the ideal phase-SCEM result (dark orange line), the reconstruction of Figure 7c (light orange line, labeled “noise-free, no extrapolation”) has the peak location offset and peak height diminished.

Given the continuity and smoothness evident in Figures 7a and 7b, we propose the following approach to improve the initialization of the dark field region elements: perform phase retrieval for the bright field region, apply a polynomial fit to the bright field region of each $S_{\mathbf{h}+\mathbf{G},\mathbf{h}}$ “disk,” extrapolate the fit

into the dark field for each of the significant \mathbf{G} beams, and use the result as the initialization for a second pass through the phase retrieval algorithm including the dark field region. Since the present case includes slight phase curvature within each disk, we limited the polynomial fit to third-order in h_x and h_y , handling the real and imaginary components of $S_{\mathbf{h}+\mathbf{G},\mathbf{h}}$ separately. The result is shown in Figure 7d, which is seen to agree well with Figure 7b, demonstrating the potential for using dark field information from 4D-STEM data, at least for thin specimens.

Figures 7b–7d present the proof-of-principle strategy on noise-free simulations. However, reliable reconstructions using the dark field region are further limited when noise is included: the low intensity in the dark field region relative to the bright field region means that a dose level adequate for successful phase retrieval of S -matrix elements in the bright-field region may not be sufficient for successful phase retrieval of S -matrix elements in the dark field region. Given the $1/\sqrt{N}$ scaling of Poisson counting statistics, if the dark field signal is a factor of 10 weaker than the bright field signal, then we should expect to need a dose level 100 times larger than what suffices for the bright field to obtain similar signal-to-noise in the dark field. Consequently, reconstructions using the dark field region for the 27 Å thickness, $\alpha_1 = 20$ mrad and $\alpha_2 = 30$ mrad fail for the low and high dose cases. The very high dose level of 1,000 C/cm² proves necessary to reconstruct the dark field and thus take advantage of the improved depth resolution from using dark field signals. Figure 7e shows the parallax reconstructions for the very high

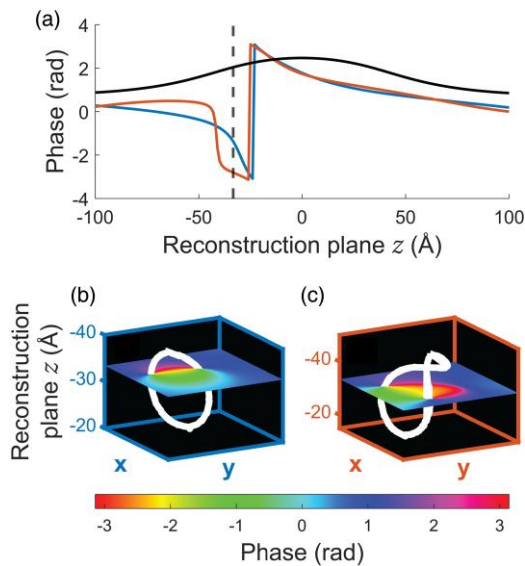


Fig. 8. Examples of phase singularity formation in the parallax reconstruction from a 92 Å thick Bi-doped sample imaged using 10 C/cm². **(a)** Line scans taken as a function of reconstruction depth along the doped atomic column. The colored lines represent two instances of singularity formation observed during our noisy 4D-STEM reconstructions. The solid black profile gives the ideal phase-SCEM result. **(b, c)** Depth slices through the 3D parallax reconstruction for the depth ($z = -33.4$ Å) indicated by the dashed vertical line in (a). Each of the boxes has been colored according to the corresponding noisy realization line scan above it. We track the vortex–antivortex pairs across the given range of reconstruction planes to form the nodal loops indicated in white.

dose case from 100 noise realizations using the extrapolation initialization method agree well with the ideal phase-SCEM result.

Explorations (not shown) for a 92 Å thick case were less successful, the increasingly fine features in the scattering matrix making low order polynomial extrapolation less reliable. Furthermore, as thermal diffuse scattering electrons become an increasingly appreciable contribution to the intensity, the phase retrieval problem becomes less consistent and so the scattering matrix determination less reliable. Figure S6 in the Supplementary Material compares the diffraction pattern intensity from elastic scattering and from elastic plus thermal scattering, showing the contribution from thermal scattering to become appreciably beyond about 25 mrad for a 92 Å thick sample.

Discussion

Our results indicate that while shot noise on 4D-STEM data may reduce the visibility of dopants relative to the supporting matrix, the depth resolution is largely unchanged relative to weak objects. However, our explorations identified some circumstances where parallax reconstruction may give a misleading impression of sample structure.

Phase Vortices

Although not readily apparent in Figures 5 or 6, phase singularities arise in the noisy simulations, specifically the creation and annihilation of vortex–antivortex pairs (Nye et al., 1974). This is not inherent to the phase-SCEM imaging geometry in general, but rather a possible consequence of the asymmetry introduced by shot noise.

For a 92 Å thick crystal at a dose of 10 C/cm² for $\alpha_1 = \alpha_2 = 20$ mrad, Figure 8a shows two parallax reconstruction difference profiles where singularities were seen to form, two colored line profiles that cannot be simply unwrapped to resemble the ideal phase-SCEM result (black line). The reasons for this become evident by looking at the 3D parallax reconstructions around the dopant-containing column. As seen in depth slices shown in Figures 8b and 8c for each of the profiles, vortex–antivortex pairs are present. Tracking these vortices in 3D produces the nodal loop maps shown as thick white lines.

Across the 100 noise realizations for each choice of parameters, phase singularities were infrequently observed, occurring with probability <1% overall. Moreover, they can be readily identified and potentially avoided: simply re-running the phase retrieval algorithm on the same set of noisy data but varying the hyperparameters or perturbing the initialization used to seed the phase retrieval may be sufficient to avoid the local minima that the phase singularities represent.

Phase-Contrast Reversal

Another challenge to interpretation of parallax reconstructions, though not occurring in the results of Figures 5 or 6, is that phase-SCEM (and, by extension, parallax phase reconstruction) can undergo contrast reversal for particularly thick or strongly scattering samples. An example is shown in Figure 9a: in this through-focal phase-SCEM image simulation of a 78 Å thick SrTiO₃ sample, the TiO column in the image center does not have the cigar-shape of the more weakly scattering Si columns in Figure 3, but instead a dip at the column center. A defocus line profile through the center of the atom would show a trough rather than a peak. A horizontal slice through the column center would show an annulus of greater phase surrounding a pronounced dip centered on the atomic column. Such caldera-like profiles seem to be a common feature in phase reconstruction methods as their underpinning assumptions break down for thicker samples (Close et al., 2015; Yang et al., 2017; Bosch & Lazić, 2019; Gao et al., 2022). Detailed interpretation of dynamical diffraction is difficult, but the qualitative behavior seen in Figure 9a also occurs in the phase object approximation for an isolated, rotationally symmetric TiO column, and with those approximations we can gain some insight into one way such contrast reversal may arise.

For a rotationally symmetric potential at $r = 0$, equation (8) (the phase-SCEM wavefield in the phase object approximation), reduces to the overlap integral

$$\psi(r=0, \Delta f) = 2\pi \int e^{i\sigma V(r')} P_1(r', \Delta f) P_2^*(r', \Delta f) r' dr'. \quad (15)$$

Evaluated via equation (15), Figure 9b shows the phase-SCEM profile through an isolated TiO column as a function of reconstruction depth for two thicknesses. Because the phase object approximation is assumed, all interaction is confined to a single plane—varying thickness simply varies the strength of the scattering within that plane. For larger Δf values, we see close agreement between the two profiles, but they diverge for Δf values near the origin: at 70 Å thickness, the profile shows the now-familiar peak at the atomic site; at 74 Å thickness, the phase along the column shows a trough.

We can understand both the contrast reversal and the suddenness of the change by visualizing the integral in equation (15) as a discrete sum of phasors. Figure 9c shows the phasor

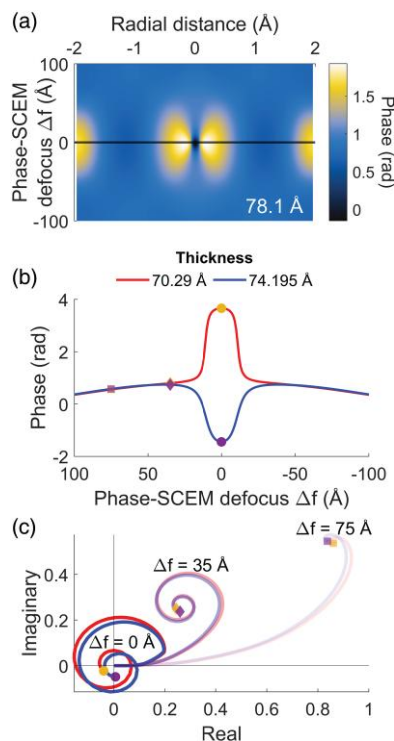


Fig. 9. (a) Multislice phase-SCEM calculation of unit cell SrTiO_3 , 78 Å thick. The central feature is the combined TiO column, showing phase-contrast reversal as it forms an annulus. (b) Line scans taken from phase-object calculations of the TiO column using equation (15). Only a single unit cell apart in assumed thickness, they demonstrate the abrupt transition from accumulated phase to a trough as the contrast reverses. (c) The phasor sum used to calculate the phase-object wavefield, showing the transformation as a function of focus depth. Minor perturbations initially have no substantive effect on the phases as marked by the agreements in the square scatter points in (b) at 75 Å. Near the sample mid-plane however, these minor differences begin to manifest in increasingly prominent ways, beginning to diverge around 35 Å (as marked by the diamonds). They reach a maximum in the middle of the sample where, so close to zero in the Argand plane, these small differences in integration result in a large phase change.

sum in the complex plane, where each discrete $e^{i\sigma V(r')} P_1(r', \Delta f) P_2^*(r', \Delta f) dr'$ element is added tip-to-tail, vector-fashion, such that the result of the integral is indicated by the end-point of each curve. The faintest curves terminating in the square symbols correspond to $\Delta f = 75$ Å—the curling at the end indicates some interference, but the terms here are mostly adding in phase. The second faintest curves terminating in the diamond symbols correspond to $\Delta f = 35$ Å—here the spiral indicates appreciable destructive interference within the integral. The solid curves terminating in the circle symbols correspond to $\Delta f = 0$ Å—now the spiral shows a high degree of destructive interference, such that the result of the integral is close to zero. The phase of the integral, which is the phase-SCEM signal, is the polar angle at the symbol point in Figure 9c. Tracking the phase of the yellow symbols (the 70 Å thickness case), one sees that it increases, slowly for large Δf but rapidly for defocus values near zero, and is always positive because it passes above the origin of the Argand diagram. Tracking the phase of the purple symbols (the 74 Å thickness case), one sees that it initially increases for large Δf , but then rapidly decreases and becomes negative: it passes below the origin of the Argand diagram. The divergence in phase seen near $\Delta f = 0$ Å in Figure 9b reflects this difference in how the

points at the two integrals' termini pass the origin in Figure 9c: near the origin, even minor perturbations in the complex numbers can result in pronounced differences in phase. This sensitivity is in some sense an artifact of constructing the phase: that the difference in the SCEM wavefield with the small change in thickness from 70 to 74 Å is modest is evident by the close proximity between the yellow and purple symbols in Figure 9c.

Because of the approximations made in equation (15), Figures 9b and 9c do not necessarily portray a complete explanation of the effects at play in the full phase-SCEM simulation in Figure 9a. Nevertheless, the possibility of sensitive phase changes when the modulus of the SCEM wavefield is small constitutes one general way that contrast reversal might come about. Since the modulus is one on the left-hand side of equation (6), which is the basis of the parallax reconstruction interpretation, it is perhaps unsurprising that when the modulus of the right-hand side is not close to one we should be cautious about assuming its phase will still closely reflect the sample potential. This then should be a check on parallax reconstructions: though our interpretation is based primarily on the phase, inspection of the modulus is prudent and in regions where that is small, one should be especially wary of the interpretation of the phase.

Further Experimental Limitations

We have explored the consequences of shot noise in some detail, and the consequences of thermal diffuse scattering briefly. However, other effects, such as scan distortion and spatial and temporal incoherence, have not been explored here. These effects introduce some degree of inconsistency in the phase retrieval step needed to determine the scattering matrix, and so would be expected to adversely impact parallax reconstruction. Previous experimental demonstrations of scattering matrix reconstruction (Brown et al., 2018, 2022; Pelz et al., 2021) achieved reasonable results despite either neglecting these effects or else mitigating them via preprocessing. This suggests that, provided these potentially deleterious effects are managed or accounted for in the processing, they should not prove too prohibitive. As noted earlier for the larger aperture case, in our experience data from multiple defocus values helps improve the robustness of phase retrieval in such cases.

Conclusion

Having established a mathematical equivalence between the parallax method of Ophus et al. (2019) and a hypothetical SCEM setup with a phase-sensitive point detector (dubbed phase-SCEM), we have derived contrast transfer and point spread functions for weakly scattering objects. When only bright field information is used in the scattering matrix determination step of the parallax method, these transfer functions and the resultant resolution is equivalent to that of depth sectioning using traditional imaging modes like ADF and DPC, though 3D imaging in those modes requires imaging across the full range of defocus values of interest, whereas the depth sectioning in the parallax method is synthesized based on scattering matrix reconstruction from 4D-STEM data from only a handful of defocus values. However, the transfer functions show that if signal from the dark field region can be used then the depth resolution can be enhanced for the same probe-forming aperture semi-angle.

In absorptive multislice phase-STEM simulations of doped Si, we show that the depth resolution of dopants is largely insensitive to the dynamical diffraction from the surrounding crystal matrix. Using only one or two through-focal 4D-STEM datasets, we further demonstrate that shot noise, a fundamental experimental limitation, may prevent reliable detection depending on dopant species and dose, not because the resolution properties are affected but because an individual noise realization introduces spurious oscillations that may be of comparable magnitude to the signal from dopants. To improve the depth resolution by using signal from the dark field region in the parallax method, we identify two impediments. One is of principle: a lack of *a priori* constraint in the relative phasing between the bright field and dark field regions, that in thin samples we show may be overcome by extrapolation from the bright field region. The other is of practice: very high doses may be needed to achieve reliable phase reconstructions in the dark field. Finally, we showed that phase singularities and caldera-like features arise in some circumstances, and describe how these complications to interpreting the parallax reconstructions can be identified.

Supplementary Material

To view supplementary material for this article, please visit <https://doi.org/10.1093/micmic/ozad068>.

Financial Support

This research is supported by an Australian Government Research Training Program Scholarship. This research was supported under the Discovery Projects funding scheme of the Australian Research Council (Project No. FT190100619). Work at the Molecular Foundry was supported by the Office of Science, Office of Basic Energy Sciences, of the U.S. Department of Energy under Contract No. DE-AC02-05CH11231.

Conflict of Interest

The authors declare that they have no competing interest.

References

- Bals S, Batenburg KJ, Liang D, Lebedev O, Van Tendeloo G, Aerts A, Martens JA & Kirschhock CEA (2009). Quantitative three-dimensional modeling of zeolite through discrete electron tomography. *J Am Chem Soc* **131**, 4769–4773.
- Bangun A, Melnykz O, März B, Diederichs B, Clausen A, Weber D, Filbir F & Müller-Caspary K (2022). Inverse multislice ptychography by layer-wise optimisation and sparse matrix decomposition. *IEEE Trans Comput Imaging* **8**, 996–1011.
- Borisevich AY, Lupini AR & Pennycook SJ (2006). Depth sectioning with the aberration-corrected scanning transmission electron microscope. *Proc Natl Acad Sci USA* **103**, 3044–3048.
- Bosch EGT & Lazić I (2019). Analysis of depth-sectioning STEM for thick samples and 3D imaging. *Ultramicroscopy* **207**, 112831.
- Brown HG, Chen Z, Weyland M, Ophus C, Ciston J, Allen LJ & Findlay SD (2018). Structure retrieval at atomic resolution in the presence of multiple scattering of the electron probe. *Phys Rev Lett* **121**, 266102.
- Brown HG, Pelz PM, Hsu SL, Zhang Z, Ramesh R, Inzani K, Sheridan E, Griffin SM, Schloz M, Pekin TC, Koch CT, Findlay SD, Allen LJ, Scott MC, Ophus C & Ciston J (2022). A three-dimensional reconstruction algorithm for scanning transmission electron microscopy

- data from a single sample orientation. *Microsc Microanal* **28**, 1632–1640.
- Bustillo KC, Zeltmann SE, Chen M, Donohue J, Ciston J, Ophus C & Minor AM (2021). 4D-STEM of beam-sensitive materials. *Acc Chem Res* **54**, 2543–2551.
- Chen Z, Jiang Y, Shao YT, Holtz ME, Odstrčil M, Guizar-Sicairos M, Hanke I, Ganschow S, Schlom DG & Muller DA (2021). Electron ptychography achieves atomic-resolution limits set by lattice vibrations. *Science* **372**, 826–831.
- Close R, Chen Z, Shibata N & Findlay SD (2015). Towards quantitative, atomic-resolution reconstruction of the electrostatic potential via differential phase contrast using electrons. *Ultramicroscopy* **159**, 124–137.
- Cosgriff EC, D'Alfonso AJ, Allen LJ, Findlay SD, Kirkland AI & Nellist PD (2008). Three-dimensional imaging in double aberration-corrected scanning confocal electron microscopy, Part I: Elastic scattering. *Ultramicroscopy* **108**, 1558–1566.
- Cosgriff E & Nellist P (2007). A Bloch wave analysis of optical sectioning in aberration-corrected STEM. *Ultramicroscopy* **107**, 626–634.
- Cowley JM (1992). Twenty forms of electron holography. *Ultramicroscopy* **41**, 335–348.
- D'Alfonso AJ, Cosgriff EC, Findlay SD, Behan G, Kirkland AI, Nellist PD & Allen LJ (2008). Three-dimensional imaging in double aberration-corrected scanning confocal electron microscopy, Part II: Inelastic scattering. *Ultramicroscopy* **108**, 1567–1578.
- Dekkers N & De Lang H (1974). Differential phase contrast in a STEM. *Optik* **41**, 452–456.
- Du M, Kandel S, Deng J, Huang X, Demortiere A, Nguyen TT, Tucoulou R, De Andrade V, Jin Q & Jacobsen C (2021). Adorym: A multi-platform generic X-ray image reconstruction framework based on automatic differentiation. *Opt Express* **29**, 10000–10035.
- Fahey PM, Griffin P & Plummer J (1989). Point defects and dopant diffusion in silicon. *Rev Mod Phys* **61**, 289.
- Findlay SD, Brown HG, Pelz PM, Ophus C, Ciston J & Allen LJ (2021). Scattering matrix determination in crystalline materials from 4D scanning transmission electron microscopy at a single defocus value. *Microsc Microanal* **27**, 744–757.
- Frank J (1992). *Electron Tomography: Three-Dimensional Imaging with the Transmission Electron Microscope*. New York: Plenum.
- Gabor D (1948). A new microscopic principle. *Nature* **161**, 777–778.
- Gao C, Hofer C, Jannis D, Béché A, Verbeeck J & Pennycook TJ (2022). Overcoming contrast reversals in focused probe ptychography of thick materials: An optimal pipeline for efficiently determining local atomic structure in materials science. *Appl Phys Lett* **121**, 081906.
- Jiang Y, Chen Z, Han Y, Deb P, Gao H, Xie S, Purohit P, Tate MW, Park J, Gruner SM, Elser V & Muller DA (2018). Electron ptychography of 2D materials to deep sub-Ångström resolution. *Nature* **559**, 343–349.
- Krajnak M & Etheridge J (2020). A symmetry-derived mechanism for atomic resolution imaging. *Proc Natl Acad Sci USA* **117**, 27805–27810.
- Lazić I, Bosch EG & Lazar S (2016). Phase contrast STEM for thin samples: Integrated differential phase contrast. *Ultramicroscopy* **160**, 265–280.
- Lichte H & Lehmann M (2007). Electron holography—Basics and applications. *Rep Prog Phys* **71**, 016102.
- Liu ACY, Neish MJ, Stokol G, Buckley GA, Smillie LA, de Jonge MD, Ott RT, Kramer MJ & Bourgeois L (2013). Systematic mapping of icosahedral short-range order in a melt-spun Zr₃₆Cu₆₄ metallic glass. *Phys Rev Lett* **110**, 205505.
- MacLaren I, Macgregor TA, Allen CS & Kirkland AI (2020). Detectors—The ongoing revolution in scanning transmission electron microscopy and why this important to material characterization. *APL Mater* **8**, 110901.
- Maiden AM, Humphry MJ & Rodenburg JM (2012). Ptychographic transmission microscopy in three dimensions using a multi-slice approach. *J Opt Soc Am A* **29**, 1606–1614.
- Müller-Caspary K, Krause FF, Grieb T, Löffler S, Schowalter M, Béché A, Galioit V, Marquardt D, Zweck J, Schattschneider P, Verbeeck J

- & Rosenauer A (2017). Measurement of atomic electric fields and charge densities from average momentum transfers using scanning transmission electron microscopy. *Ultramicroscopy* **178**, 62–80.
- Müller K, Krause FF, Béch e A, Schowalter M, Galioit V, L offler S, Verbeeck J, Zweck J, Schattschneider P & Rosenauer A (2014). Atomic electric fields revealed by a quantum mechanical approach to electron picodiffraction. *Nat Commun* **5**, 5653.
- Nye JF, Berry MV & Frank FC (1974). Dislocations in wave trains. *Proc R Soc Lond A Math Phys Sci* **336**, 165–190.
- O’Leary CM, Martinez GT, Liberti E, Humphry MJ, Kirkland AI & Nellist PD (2021). Contrast transfer and noise considerations in focused-probe electron ptychography. *Ultramicroscopy* **221**, 113189.
- Ophus C (2019). Four-dimensional scanning transmission electron microscopy (4D-STEM): From scanning nanodiffraction to ptychography and beyond. *Microsc Microanal* **25**, 563–582.
- Ophus C, Harvey TR, Yasin FS, Brown HG, Pelz PM, Savitzky BH, Ciston J & McMorrnan BJ (2019). Advanced phase reconstruction methods enabled by four-dimensional scanning transmission electron microscopy. *Microsc Microanal* **25**, 10–11.
- Oshima Y, Hashimoto Y, Tanishiro Y, Takayanagi K, Sawada H, Kaneyama T, Kondo Y, Hashikawa N & Asayama K (2010). Detection of arsenic dopant atoms in a silicon crystal using a spherical aberration corrected scanning transmission electron microscope. *Phys Rev B* **81**, 035317.
- Pelz PM, Brown HG, Stonemeyer S, Findlay SD, Zettl A, Ercius P, Zhang Y, Ciston J, Scott M & Ophus C (2021). Phase-contrast imaging of multiply-scattering extended objects at atomic resolution by reconstruction of the scattering matrix. *Phys Rev Res* **3**, 023159.
- Pennington RS, Van den Broek W & Koch CT (2014). Third-dimension information retrieval from a single convergent-beam transmission electron diffraction pattern using an artificial neural network. *Phys Rev B* **89**, 205409.
- Pennycook TJ, Lupini AR, Yang H, Murfitt MF, Jones L & Nellist PD (2015). Efficient phase contrast imaging in stem using a pixelated detector. Part 1: Experimental demonstration at atomic resolution. *Ultramicroscopy* **151**, 160–167.
- Ren D, Ophus C, Chen M & Waller L (2020). A multiple scattering algorithm for three dimensional phase contrast atomic electron tomography. *Ultramicroscopy* **208**, 112860.
- Rodenburg J & Maiden A (2019). Ptychography. In: Hawkes PW & Spence JCH (eds) *Springer Handbook of Microscopy*, Springer Handbooks, Springer, Cham, pp. 819–904.
- Savitzky A & Golay MJE (1964). Smoothing and differentiation of data by simplified least squares procedures. *Anal Chem* **36**, 1627–1639.
- Schloz M, Pekin TC, Chen Z, Van den Broek W, Muller DA & Koch CT (2020). Overcoming information reduced data and experimentally uncertain parameters in ptychography with regularized optimization. *Opt Express* **28**, 28306–28323.
- Sturkey L (1962). The calculation of electron diffraction intensities. *Proc Phys Soc (1958–1967)* **80**, 321.
- Van den Broek W & Koch CT (2012). Method for retrieval of the three-dimensional object potential by inversion of dynamical electron scattering. *Phys Rev Lett* **109**, 245502.
- Van den Broek W & Koch CT (2013). General framework for quantitative three-dimensional reconstruction from arbitrary detection geometries in TEM. *Phys Rev B* **87**, 184108.
- Voyles PM (2006). Imaging single atoms with z-contrast scanning transmission electron microscopy in two and three dimensions. *Microchim Acta* **155**, 5–10.
- Wen Y, Ophus C, Allen CS, Fang S, Chen J, Kaxiras E, Kirkland AI & Warner JH (2019). Simultaneous identification of low and high atomic number atoms in monolayer 2D materials using 4D scanning transmission electron microscopy. *Nano Lett* **19**, 6482–6491.
- Winkler F, Barthel J, Dunin-Borkowski RE & M uller-Caspary K (2020). Direct measurement of electrostatic potentials at the atomic scale: A conceptual comparison between electron holography and scanning transmission electron microscopy. *Ultramicroscopy* **210**, 112926.
- Wu RJ, Mittal A, Odlyzko ML & Mkhoyan KA (2017). Simplifying electron beam channeling in scanning transmission electron microscopy (STEM). *Microsc Microanal* **23**, 794–808.
- Xin HL, Intaraprasong V & Muller DA (2008). Depth sectioning of individual dopant atoms with aberration-corrected scanning transmission electron microscopy. *Appl Phys Lett* **92**, 013125.
- Xin HL & Muller DA (2009). Aberration-corrected ADF-STEM depth sectioning and prospects for reliable 3D imaging in S/TEM. *J Electron Microsc (Tokyo)* **58**, 157–165.
- Yang H, MacLaren I, Jones L, Martinez GT, Simson M, Huth M, Ryll H, Soltau H, Sagawa R, Kondo Y, Ophus C, Ercius P, Jing L, Kov acs A & Nellist PD (2017). Electron ptychographic phase imaging of light elements in crystalline materials using Wigner distribution deconvolution. *Ultramicroscopy* **180**, 173–179.
- Yang H, Pennycook TJ & Nellist PD (2015). Efficient phase contrast imaging in STEM using a pixelated detector. Part II: Optimisation of imaging conditions. *Ultramicroscopy* **151**, 232–239.
- Yang H, Rutte R, Jones L, Simson M, Sagawa R, Ryll H, Huth M, Pennycook T, Green M, Soltau H, Kondo Y, Davis BG & Nellist PD (2016). Simultaneous atomic-resolution electron ptychography and z-contrast imaging of light and heavy elements in complex nanostructures. *Nat Commun* **7**, 12532.
- Y ucelen E, Lazi c I & Bosch EGT (2018). Phase contrast scanning transmission electron microscopy imaging of light and heavy atoms at the limit of contrast and resolution. *Sci Rep* **8**, 1–10.
- Zhang C, Han R, Zhang AR & Voyles PM (2020). Denoising atomic resolution 4D scanning transmission electron microscopy data with tensor singular value decomposition. *Ultramicroscopy* **219**, 113123.
- Zhou L, Song J, Kim JS, Pei X, Huang C, Boyce M, Mendon a L, Clare D, Siebert A, Allen CS, Liberti E, Stuart D, Pan X, Nellist PD, Zhang P, Kirkland AI & Wang P (2020). Low-dose phase retrieval of biological specimens using cryo-electron ptychography. *Nat Commun* **11**, 2773.